Structural Analysis of Block Copolymer Thin Films with Grazing Incidence Small-Angle X-ray Scattering

Byeongdu Lee,† Insun Park, Jinhwan Yoon, Soojin Park, Jehan Kim, Kwang-Woo Kim, Taihyun Chang,* and Moonhor Ree*

Department of Chemistry, Pohang Accelerator Laboratory, Center for Integrated Molecular Systems, Polymer Research Institute, and Division of Molecular and Life Sciences (BK21 Program), Pohang University of Science & Technology, Pohang 790-784, Republic of Korea

Received November 25, 2004; Revised Manuscript Received February 25, 2005

ABSTRACT: The grazing incidence small-angle X-ray scattering (GISAXS) from structures within a thin film on a substrate is generally a superposition of the two scatterings generated by the two X-ray beams (reflected and transmitted beams) converging on the film with a difference of twice the incidence angle (α_i) of the X-ray beam in their angular directions; these two scatterings may overlap or may be distinct, depending on α_i. The two scatterings are further distorted by the effects of refraction. These reflection and refraction effects mean that GISAXS is complicated to analyze. To quantitatively analyze GISAXS patterns, in this study we derived a GISAXS formula under the distorted wave Born approximation. We applied this formula to the quantitative analysis of the GISAXS patterns obtained for various compositions of polystyrene-*b*-polyisoprene (PS-*b*-PI) diblock copolymer thin films on silicon substrates with native oxide layers. This analysis showed that the diblock copolymer thin films consist of hexagonally packed cylinder (HEX) structures, hexagonally perforated layer (HPL) structures, and gyroid structures, all with characteristic preferential orientations, depending on the composition of the copolymer. This is the first report of GISAXS studies of HEX, HPL, and gyroid microdomain structures in block copolymer thin films. Moreover, our study also provides a simple method for understanding GISAXS patterns and for determining the structure factor or interference function from them. Thus, the use of the GISAXS technique with our derived GISAXS formula as a data analysis engine is a very powerful tool for determining the morphologies of polymer thin films on substrates.

1. Introduction

The physics behind the microstructures of block copolymers has been extensively investigated over the past three decades.[1] If the covalently linked constituent polymer blocks are immiscible, phase separation is induced on a scale that is directly related to the size of the copolymer chains, typically 10−100 nm, resulting in various morphologies such as spherical, cylindrical, gyroid, and lamellar phases, depending on their block volume ratios.[1] The formation of such structures, which have usually been determined with conventional small-angle X-ray scattering (SAXS) and transmission electron microscopy (TEM), can be explained by taking into consideration the interaction energies of the block components, the variation in entropy as a function of molecular weight, and the block volume ratios.[1]

Thin films of block copolymers have recently received considerable attention because of their potential nanofabrication applications.[2,3] In these applications, controlling the morphology of the block copolymer films, particularly the orientation and ordering of the phase-separated microdomains, is essential. In the thin film state, however, surface−block interactions and the confinement effect related to film thickness give rise to morphologies that differ from those in the bulk.[2,4] By developing our understanding of thin film morphologies at a fundamental level, it is conceivable that the control of thin film morphology could be achieved by fine-tuning the surface−block interactions and the film thickness. Microscopy tools such as TEM and atomic force microscopy (AFM) are commonly used for characterizing the structures of block copolymer thin films.[5] With these tools, images such as those that show local structures near the surface have been obtained, thus enabling discussion of the underlying physics.[6] From the viewpoint of fabrication, this approach is often sufficient, but from the scientific point of view, SAXS results are required because only they provide information on a larger scale at high resolution.

Transmission SAXS (TSAXS) is a powerful method, but a high-intensity or high-energy X-ray beam (about 15 keV or higher) is required to obtain an acceptable scattering signal because the X-ray must pass through both the thin film and the much thicker substrate on which the film is deposited. Another X-ray scattering technique is grazing incidence SAXS (GISAXS), which has several important advantages over TSAXS:[7−18] (1) a highly intense scattering pattern is always obtained, even for films of nanoscale thickness, because the X-ray beam path length through the film plane is sufficiently long; (2) there is no unfavorable scattering from the substrate on which the film is deposited; and (3) sample preparation is easy. Analytical solutions of GISAXS patterns based on the distorted wave Born approximation (DWBA) have been developed to describe the complicated reflection and refraction effects,[7−18] which are not found in conventional TSAXS. GISAXS can be applicable to determine internal morphologies of thin films[9,13−17] as well as top surface morphologies of thick films and substrates.[7,8,16,18] Much effort on the GISAXS analysis of the top surface morphologies has been done so far.[7,8,18] In particular, Muller-Buschbaum[16] reported

† Present address: Experimental Facility Division, Argonne National Laboratory, Argonne, IL 60439.

* To whom all correspondence should be addressed: Tel +82-54-279-2120 (M.R.), 279-2109 (T.C.); Fax +82-54-279-3399; e-mail ree@postech.edu, tc@postech.edu.

10.1021/ma047562d CCC: $30.25
Published on Web 04/15/2005

the GISAXS study of thin films and dilute islands on substrates of a symmetric diblock copolymer. Recently, quantitative GISAXS analyses for nanoparticles in thin films were reported.[9,13] Lee et al.[9,13] and Gibaud et al.[14] reported the GISAXS analyses of the thin films composed of randomly and regularly organized nanopores, respectively. GISAXS analysis has been further applied to investigate the transitions of internal morphologies in block copolymer thin films.[17] GISAXS patterns have also been analyzed using conventional methods and ideas such as the Guinier or power law analysis, which are commonly used in analyzing TSAXS data.[12] However, both the complex analytical solution and the simple analytical approach do not make full use of the power of GISAXS to characterize structures: the former method is limited in its range of applications, and use of the latter method may result in the loss of information and misinterpretation. Moreover, a full analysis under the DWBA of GISAXS patterns for block copolymers in thin films has rarely been carried out.

In the present study, we derived a GISAXS formula under the DWBA for analysis of the structures in copolymer thin films deposited on substrates. Using the derived scattering formula, we attempted the quantitative analysis of the two-dimensional (2D) GISAXS patterns of polystyrene-*b*-polyisoprene (PS-*b*-PI) diblock copolymer films deposited on silicon substrates, which were obtained with synchrotron radiation sources. The analysis of the GISAXS patterns was successfully carried out, and we found that PS-*b*-PI thin films deposited on silicon substrates contain hexagonally packed cylinder (HEX) structures, hexagonally perforated layer (HPL) structures, and gyroid structures, all with characteristic preferential orientations, depending on the composition of the copolymer. This is the first report of detailed GISAXS studies of HEX, HPL, and gyroid microdomain structures in block copolymer thin films deposited on substrates and demonstrates that the use of the GISAXS technique with the derived scattering formula as a data analysis engine is a very powerful method for determining the morphologies of thin films deposited on substrates.

2. Calculation of the GISAXS Patterns Resulting from Various Thin Film Morphologies

2.1. GISAXS Intensity. Consider the thin film containing particles on a substrate depicted in Figure 1a. According to the distorted wave Born approximation (DWBA),[7−18] the scattering potential V of such a thin film can be written as the superposition of two terms:

$$V = V_1 + V_2 \tag{1}$$

where V_1 is the scattering potential of a thin film without particles on a thick substrate with flat interfaces and V_2 is that of the particles in the film, which is very small compared to V_1 and can be treated as its perturbation. The only condition that must be satisfied by a division of the scattering potential is that the following wave equation should be solvable exactly:

$$(\nabla^2 + {k_0}^2 - V_1)\Psi = 0 \tag{2}$$

where Ψ is the amplitude of the scattered wave and k_0 is the modulus of the wave vector.

The exact solution for the unperturbed system can be obtained using the Parratt formalism.[19] The solutions

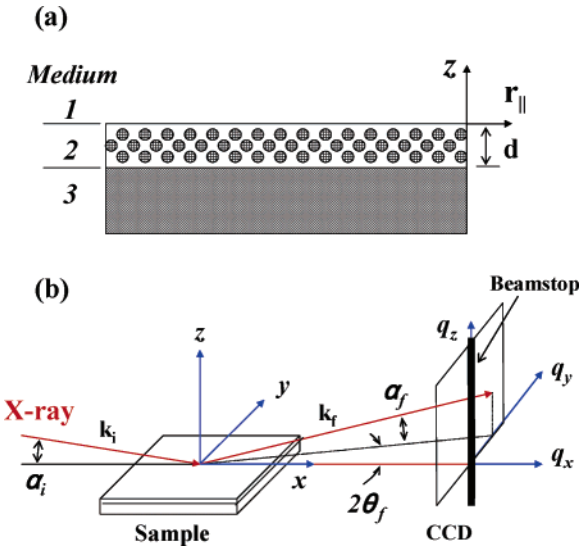

Figure 1. (a) A schematic diagram of the structure of a block copolymer film deposited on a silicon substrate: medium 1, vacuum; medium 2, block copolymer thin film; medium 3, silicon substrate with infinite thickness. d is the thickness of medium 2 (i.e., the block copolymer film). (b) Geometry of GISAXS: α_i is the incident angle at which the X-ray beam impinges on the film surface; α_f and $2\theta_f$ are the exit angles of the X-ray beam with respect to the film surface and to the plane of incidence respectively; $\mathbf{k}_i$ and $\mathbf{k}_f$ are the wave vectors of the incident and exit X-ray beams, respectively; q_x, q_y, and q_z are the components of the scattering vector $\mathbf{q}$; a strip-shaped beam stop was used to block the strong specular reflection of the X-ray beam and diffuse scattering along the α_f axis.

for the X-ray wave in the unperturbed system are as follows:

$$\Psi_1^1(\mathbf{r}) = e^{i\mathbf{k}_{||}\mathbf{r}_{||}}(e^{ik_{z,1}z} + R_1 e^{-ik_{z,1}z}) \qquad z > 0 \tag{3a}$$

$$\Psi_2^1(\mathbf{r}) = e^{i\mathbf{k}_{||}\mathbf{r}_{||}}(T_2 e^{ik_{z,2}z} + R_2 e^{-ik_{z,2}z}) \qquad 0 > z > -d \tag{3b}$$

$$\Psi_3^1(\mathbf{r}) = e^{i\mathbf{k}_{||}\mathbf{r}_{||}} T_3 e^{ik_{z,3}(z+d)} \qquad -d > z \tag{3c}$$

where R_j and T_j are the amplitudes of the outgoing and incoming waves in medium j, respectively, and d is the film thickness (Figure 1a). $k_{||}$ and $k_{z,j}$ are the parallel and perpendicular components of the incident wave in medium j, respectively. $k_{z,j} = k_i\sqrt{{n_j}^2 - \cos^2\alpha_i}$, where α_i is the glancing angle of incidence, $k_i = -2\pi/\lambda = -k_0$ (λ, the wavelength of the X-ray beam), and $n_j = 1 - \delta_j + i\beta_j$ with a dispersion δ_j and an absorption β_j. Since we are interested in the scatterings in medium 2 in which particles are present (Figure 1a), $\Psi_2^1(\mathbf{r})$ will be written as $\Psi_i(\mathbf{r})$. To indicate that it is an incoming wave, the wave vector $k_{z,2}$ is written as $k_{z,i}$ and $k_{z,f}$ denotes the wave vector of the outgoing scattered wave in medium 2. The other eigenstate, i.e., the scattered wave, can be represented by a time reversal state of the incoming wave:

$$\Psi_f(\mathbf{r}) = e^{i\mathbf{k}_{||}\mathbf{r}_{||}}(T_2^* e^{ik^*_{z,f}z} + R_2^* e^{-ik^*_{z,f}z}) \tag{4}$$

Taking these solutions $\Psi_i(\mathbf{r})$ and $\Psi_f(\mathbf{r})$ into account, the perturbation V_2 can be expressed as follows:

$$\Psi_{sc}(r) = -\frac{e^{ik_0 r}}{4\pi r}\int \Psi_f^*(\mathbf{r})\, V_2 \Psi_i(\mathbf{r}) \tag{5}$$

where $\Psi_{sc}(r)$ is the amplitude of the scattered wave. To clarify whether the X-ray wave is incoming or outgoing, T_2, T_2^*, R_2, and R_2^* are rewritten as T_i, T_f^*, R_i, and R_f^*, respectively. The superscript * indicates the complex conjugate. After inserting eqs 3b and 4 into eq 5 and carrying out rigorous algebra, one can obtain the following equation for the amplitude of the scattered wave:

$$\Psi_{sc}(r) = -\frac{e^{ik_0 r}}{4\pi r}\int d^2 r'_{||} e^{-iq_{||}r'_{||}}[T_i T_f \int_{-d}^{0} dz' e^{-iq_{1,z}z'} V_2(r'_{||},z') + T_i R_f \int_{-d}^{0} dz' e^{-iq_{2,z}z'} V_2(r'_{||},z') + T_f R_i \int_{-d}^{0} dz' e^{-iq_{3,z}z'} V_2(r'_{||},z') + R_i R_f \int_{-d}^{0} dz' e^{-iq_{4,z}z'} V_2(r'_{||},z')] \quad (6)$$

where $q_{1,z} = k_{z,f} - k_{z,i}$, $q_{2,z} = -k_{z,f} - k_{z,i}$, $q_{3,z} = k_{z,f} + k_{z,i}$, and $q_{4,z} = -k_{z,f} + k_{z,i}$. Equation 6 can also be expressed in the following simpler form:

$$\Psi_{sc}(r) = -\frac{e^{ik_0 r}}{4\pi r}(T_i T_f F(q_{||},q_{1,z}) + T_i R_f F(q_{||},q_{2,z}) + T_f R_i F(q_{||},q_{3,z}) + R_i R_f F(q_{||},q_{4,z})) \quad (7)$$

where F is the amplitude of scattering from the particles in the film and $q_{||} = \sqrt{{q_x}^2 + {q_y}^2}$. Here, the size of the particles is assumed to be small compared to the film thickness d.

The intensity (I_{GISAXS}) of the wave scattered from the thin film sample (i.e., medium 2 in Figure 1a) can then be expressed as follows:

$$I_{GISAXS} = \frac{d\sigma}{d\Omega} = r^2\{\Psi_{sc}(r)\ \Psi_{sc}^*(r)\} = \frac{1}{16\pi^2}(I_{independent} + I_{cross}) \quad (8)$$

where $d\sigma/d\Omega$ is the differential cross section of the film, and $I_{independent}$ and I_{cross} are the independent scattering and cross terms, respectively.

Since $q_{j,z}$ has an imaginary term when α_i and/or α_f are smaller than $\alpha_{c,f}$, such imaginary terms should be taken into account in the derivation of eq 8. Indeed, the imaginary terms of all q_z components can be written as $\mathrm{Im}(q_z) = |\mathrm{Im}(k_{z,f})| + |\mathrm{Im}(k_{z,i})|$.

Taking the approximation of all q_z components into account, F in eq 7 can be treated as a simple Fourier transform of the scattering potential.[13] Therefore, I_{GISAXS} (i.e., eq 8) can be rewritten by the following simplified expression:

$$I_{GISAXS}(\alpha_f,2\theta_f) = \frac{1}{16\pi^2}\frac{1-e^{-2\mathrm{Im}(q_z)d}}{2\mathrm{Im}(q_z)}|T_i T_f F(q_{||},\mathrm{Re}(q_{1,z})) + T_i R_f F(q_{||},\mathrm{Re}(q_{2,z})) + T_f R_i F(q_{||},\mathrm{Re}(q_{3,z})) + R_i R_f F(q_{||},\mathrm{Re}(q_{4,z}))|^2 \quad (9)$$

where $2\theta_f$ is the angle between the scattered beam and the plane of incidence (i.e., in-plane exit angle) and $\mathrm{Re}(x)$ is the real part of x. As shown in Figure 1b, the detector plane is defined by rectangular coordinates with two perpendicular axes, α_f and $2\theta_f$.

Here it is worth considering the ensemble average of the scattered intensities from particles in the film over the particle size distribution and other parameters related to the film and the scattering measurement. The ensemble average of $I_{independent}$ (in eqs 8 and 9) can be performed in a straightforward manner because $I_{independent}$ is always positive; the ensemble average of the scattered intensities of particles is well described in the literature.[9−11] In contrast to $I_{independent}$, the ensemble average of I_{cross} should be performed with care because I_{cross} may be positive or negative depending on several factors. First, the parameter R_i in the expression for I_{cross} may be positive or negative depending on the incident angle of the X-ray beam, the refractive index and thickness of the film, the particle size distribution, and the divergence of the incident X-ray beam. Second, the products of F terms and their complex terms in the expression for I_{cross} are not always in the same phase. The frequency of the phase (i.e., positive or negative) variation becomes faster as the film thickness increases. These products also vary depending on the particle size distribution and are additionally sensitive to any incoherence in the incident X-ray beam. Because of the contributions of these factors, the ensemble average of I_{cross} either vanishes completely or is sufficiently small that it can be neglected. However, in the case of a film containing monodisperse particles and a coherent X-ray beam, the ensemble average of I_{cross} cannot be neglected.

In $I_{independent}$ of eq 8 or 9 the complex product $|F(q_{||},q_{j,z})|^2$ term contains the complex scattering vector component q_z. As previously described elsewhere,[13] the $|F(q_{||},q_{j,z})|^2$ term can be obtained as the following expression:

$$|F(q_{||},q_{j,z})|^2 = \frac{1-e^{-2\mathrm{Im}(q_{j,z})d}}{2\mathrm{Im}(q_{j,z})} I_1(q_{||},\mathrm{Re}(q_{j,z})) \quad (10)$$

where I_1 is the scattered intensity from the particles in the film. Therefore, for the films of which the ensemble average of I_{cross} can be negligible, I_{GISAXS} (i.e., eq 9) can be approximated by the following expression:

$$I_{GISAXS}(\alpha_f,2\theta_f) \cong \frac{1}{16\pi^2} I_{independent} = \frac{1}{16\pi^2}\frac{1-e^{-2\mathrm{Im}(q_z)d}}{2\mathrm{Im}(q_z)}[|T_i T_f|^2 I_1(q_{||},\mathrm{Re}(q_{1,z})) + |T_i R_f|^2 I_1(q_{||},\mathrm{Re}(q_{2,z})) + |T_f R_i|^2 I_1(q_{||},\mathrm{Re}(q_{3,z})) + |R_i R_f|^2 I_1(q_{||},\mathrm{Re}(q_{4,z}))] \quad (11)$$

For a given film system, the overall GISAXS pattern generated by eq 9 is nearly the same as that generated by eq 11. However, the GISAXS pattern generated by eq 9 more clearly shows the oscillation frequency arising from the thickness of the film. On the other hand, when the analytical formula for the scattering amplitudes is not easily obtained, eq 11 is very useful for calculating scattering intensities from particles in thin films even though the cross terms give rise to some minor error in the intensity near the critical angle. Therefore, one can use either eq 9 or 11, depending on the circumstances.

An important consideration in GISAXS analysis is that if the diffraction spots are symmetric over the equatorial plane in the GISAXS pattern, they can be understood as two sets generated by two incident beams. Because of the symmetry over the equatorial plane, the patterns along the q_z and $-q_z$ are the same (Figure 2).

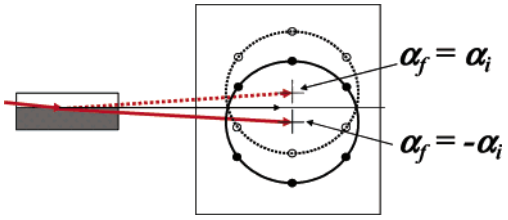

Figure 2. A schematic GISAXS pattern due to HEX-structured microdomains in the in-plane of a diblock copolymer thin film deposited on a silicon substrate: the six open spots are the first-order diffraction peaks generated by the reflected X-ray beam (marked with the dotted arrow); the six filled spots are the first-order diffraction peaks generated by the transmitted X-ray beam (marked with the solid arrow); the dotted and solid cross marks denote positions of the specularly reflected and transmitted X-ray beams, respectively.

Thus, the $q_{1,z}$ and $q_{4,z}$, whose lengths are the same but directions are opposite, become overlapped. The values of $q_{2,z}$ and $q_{3,z}$ are the same. Thus, the diffraction spots from the first and last terms overlap exactly, and the other two terms also overlap exactly. In the case of $q_{1,z}$ and $-q_{4,z}$, the incident beam direction is downward to the film, and the same with the transmitted beam. In the other case of $-q_{2,z}$ and $q_{3,z}$, however, the reflected beam works as the source of diffraction peaks or the incident beam. When $k_{z,\mathrm{f}}$ is $k_{z,\mathrm{i}}$, $q_{1,z}$ and $q_{4,z}$ become zero, which means the direction of $k_{z,\mathrm{i}}$ is the zero angle position for the scattering along $q_{1,z}$ and $q_{4,z}$. On the other hand, when $k_{z,\mathrm{f}}$ is $-k_{z,\mathrm{i}}$, $q_{2,z}$ and $q_{3,z}$ become zero, which means the direction of $-k_{z,\mathrm{i}}$ is the zero angle position for the scattering along $q_{2,z}$ and $q_{3,z}$. As a result, the four scattering terms can be considered as only two terms: the scattering around the transmitted beam ($k_{z,\mathrm{i}}$) and the scattering around the reflected beam ($-k_{z,\mathrm{i}}$). Conclusively, the GISAXS pattern can be considered as the overlap of scatterings centered on the transmitted beam position and those centered on the reflected beam position. This realization makes the interpretation of GISAXS patterns much easier. A schematic example is shown in Figure 2 where two sets of six first-order diffraction peaks for a HEX structure in a thin film deposited on a substrate are marked with their source beams; the group of six filled spots on the solid circle are from the transmitted beam, and the other group of six open spots on the dotted circle are from the reflected beam. In fact, GISAXS patterns can be understood as the superposition of two SAXS patterns generated by two X-ray beam sources (i.e., the reflected and transmitted beams) converging on the sample with a $2\alpha_{\mathrm{i}}$ difference in their angular direction; however, the reflected beam need not be considered when α_{i} is larger than the critical angle of the substrate because the reflected beam intensity is greatly reduced. As can be seen in Figure 2, the two groups of diffraction spots can overlap or be distinct from each other, depending on the incident angle α_{i}. Thus, the structure of the thin film can be analyzed using only one group of scattering spots after proper refraction correction, as is carried out in conventional TSAXS.

2.2. Intensity of Scattering from Particles in a Thin Film. For particles with a polydisperse size distribution in a thin film, the scattering intensity of the particles, I_1, in eq 11 can be expressed as the product of the structure factor $S(\mathbf{q})$ and form factor $P(\mathbf{q})$ of the particles under a local monodisperse approximation:[20]

$$I_1(\mathbf{q}) = S(\mathbf{q})\, P(\mathbf{q}) \tag{12}$$

The term $S(\mathbf{q})$ provides information on particle positions such as the crystal lattice parameters, orientation, dimension, and symmetry in a crystalline solid or the interparticle distances in an isotropic colloid-like system, whereas the term $P(\mathbf{q})$ describes the shape, size, and orientations of the particles. The analytical amplitudes and intensities of the form factors are known for several different particle shapes.[11,21] The structure factors $S(\mathbf{q})$ of isotropic colloid-like systems are also available in the literature.[11,21] Unfortunately, unless the particles are positioned in crystal-like positions, it is only rarely possible that the amplitude of the structure factor can be derived, and the intensity has thus only been analytically calculated in very few cases. Equation 11 is more convenient than eq 7 (or eq 9) since it can be used whether or not the ordering of the particles is crystal-like, as explained in the previous section.

In this study, we focused on crystalline and paracrystalline systems. The structure factors $S(\mathbf{q})$ of a crystalline system can be calculated using its crystallographic information, whereas the $S(\mathbf{q})$ of a paracrystalline system can be calculated from paracrystal models. Further, we were interested in this study in the orientations of the crystalline domains as well as of lattice structures with introducing their rotation matrices. These subjects are discussed in detail in the following subsections.

2.2.1. Calculation of the Structure Factor from Crystallographic Information. For a crystalline system, $S(\mathbf{q})$ can easily be calculated from its lattice parameters and space group as follows.

$$S(\mathbf{q}) = |F_{\mathrm{c}}(\mathbf{q})\, Z(\mathbf{q})|^2 \tag{13}$$

where

$$F_{\mathrm{c}}(\mathbf{q}) = \sum_j \mathrm{e}^{i\mathbf{q}\cdot\mathbf{r}_j} \tag{14}$$

and

$$Z(\mathbf{q}) = K \sum_{h=-\infty}^{\infty} \sum_{k=-\infty}^{\infty} \sum_{l=-\infty}^{\infty} \delta\left(\frac{\mathbf{q}}{2\pi} - \mathbf{r}^*_{hkl}\right) \tag{15}$$

where $F_{\mathrm{c}}(\mathbf{q})$ and $Z(\mathbf{q})$ are the geometrical structure factor and lattice factor, respectively, the index j is defined such that $\mathbf{r}_j$ is a vector terminating at scattering center j in the unit cell, K is a proportionality constant, and δ is a delta function. $\mathbf{r}^*_{hkl}$ denotes the reciprocal lattice point given by

$$\mathbf{r}^*_{hkl} = h\mathbf{a}^*_1 + k\mathbf{a}^*_2 + l\mathbf{a}^*_3 \tag{16}$$

where $\mathbf{a}^*_1$, $\mathbf{a}^*_2$, and $\mathbf{a}^*_3$ are the basis vectors of the reciprocal lattice.

The full calculation requires some other parameters, including parameters to account for finite crystal size, temperature, and resolution effects, and the use of some related theories, which can easily be found in the literature.[22] In this paper, several cubic structures and two-dimensional (2D) hexagonal structures are of interest; the space group for body-centered-cubic (bcc) structures is assumed to be *Pnam*, *Fm*-3*m* for face-centered-cubic (fcc) structures, and *Ia*-3*d* for gyroid structures.

2.2.2. Calculation of the Structure Factor from a Paracrystal Model. For a paracrystal system, the structure factor $S_{\mathrm{p}}(\mathbf{q})$, which is also known as the

interference function or lattice factor, can be determined from the Fourier transform of a complete set of lattice points. In this sense, $S_p(\mathbf{q})$ is the same as that defined in the previous subsection. However, the paracrystal model assumes to have the second kind of crystal imperfection, so its lattice points are no longer fixed at certain positions but instead are described by a positional distribution function. In the simple case where the autocorrelation function of a crystal lattice is given by the convolution product of the distributions of the lattice points along three axes and the distribution function is a Gaussian, $S_p(\mathbf{q})$ can be expressed by the following equation:

$$S_p(\mathbf{q}) = \prod_{k=1}^{3} Z_{p,k}(\mathbf{q}) \tag{17}$$

where

$$Z_{p,k}(\mathbf{q}) = 1 + \frac{F_{p,k}(\mathbf{q})}{1 - F_{p,k}(\mathbf{q})} + \frac{F^*_{p,k}(\mathbf{q})}{1 - F^*_{p,k}(\mathbf{q})} \tag{18}$$

$$F_{p,k}(\mathbf{q}) = |F_{p,k}(\mathbf{q})| e^{-i\mathbf{q}\cdot\mathbf{b}_k} \tag{19}$$

$$|F_{p,k}(\mathbf{q})| = e^{-(1/2)\Delta b_k{}^2 q^2} \tag{20}$$

Here, $\mathbf{b}_k$ and $\Delta\mathbf{b}_k$ are the fundamental vectors of the kth axis and its displacement.

In this study, isotropic displacement is assumed and the domain orientation is accounted for numerically (see the next subsection). The expressions in eqs 17 and 18 for 2D hexagonal structures[22] are slightly different from those for cubic structures[23] because of the different definitions of their autocorrelation functions for the symmetry of the diffraction peak intensities. However, the approach to treating displacements in 2D hexagonal structures along the axis is basically the same as that used for cubic structures.

2.3. Positions of Scattering Peaks in the Detector Plane for Randomly Oriented Structure. When the structure of a film is randomly oriented in the plane of the film but epitaxially ordered out of plane, the peak position vector $\mathbf{q_c}$ of a certain reciprocal lattice point $\mathbf{c}^*$ in the same reciprocal lattice is given by

$$\mathbf{q_c} = \mathbf{R}\cdot\mathbf{c}^* \equiv (q_{c,x}, q_{c,y}, q_{c,z}) \tag{21}$$

where $\mathbf{R}$ is a 3 × 3 rotation matrix to decide the preferred orientation of the structure in the film, and $q_{c,x}$, $q_{c,y}$, and $q_{c,z}$ are the x, y, and z components of the peak position vector $\mathbf{q_c}$, respectively. Using eq 21, every peak position can be obtained. Because of cylindrical symmetry caused by the random orientation in the plane of film, the Debye−Scherrer ring composed of the in-plane randomly oriented $\mathbf{c}^*$ cuts an Ewald sphere at two points in its top hemisphere: $q_{||} = q_{c,||} \equiv \pm\sqrt{q_{c,x}{}^2 + q_{c,y}{}^2}$ with $q_z = q_{c,z}$. Thus, diffraction patterns with cylindrical symmetry are easily calculated in $\mathbf{q}$ space. It is then convenient to determine the preferred orientation of known structures and further to analyze anisotropic SAXS patterns. However, since $\mathbf{q}$ space is distorted in GISAXS by refraction and reflection effects, the relation between the detector plane expressed as the Cartesian coordinate defined by two perpendicular axes (i.e., by the in-plane exit angle $2\theta_f$ and the out-of-plane exit angle α_f) and the reciprocal lattice points is needed. The two wave vectors $k_{z,i}$ and $k_{z,f}$ are corrected for refraction as $k_0\sqrt{n^2 - \cos^2\alpha_i}$ and $k_0\sqrt{n^2 - \cos^2\alpha_f}$, respectively; n is the refractive index of the film. Therefore, the two sets of diffraction peaks that result from the incoming and outgoing X-ray beams, as explained in section 2.1, and denoted by q_1 and q_3, respectively, are given at the exit angles by the following expression:

$$\alpha_f = \arccos\left(\sqrt{n^2 - \left(\frac{q_{c,z}}{k_0} \pm \sqrt{n^2 - \cos^2\alpha_i}\right)^2}\right) \tag{22}$$

where $q_{c,z}/k_0 > \sqrt{n^2 - \cos^2\alpha_i}$. In eq 22, the positive sign denotes diffraction peaks produced by the outgoing X-ray beam, and the negative sign denotes diffraction peaks produced by the incoming X-ray beam. The in-plane incidence angle $2\theta_i$ is usually zero, so the in-plane exit angle $2\theta_f$ can be expressed as follows:

$$2\theta_f = \arccos\left(\frac{\cos^2\alpha_i + \cos^2\alpha_f - \left(\frac{q_{c,||}}{k_0}\right)^2}{2\cos\alpha_i\cos\alpha_f}\right) \tag{23}$$

Therefore, diffraction spots detected on the detector plane in GISAXS measurements can be directly compared to those derived using eqs 21−23 from an appropriate model and thus analyzed in terms of the model.

Table 1. Molecular Weights and Compositions of the PS-*b*-PI Diblock Copolymers

diblock copolymer	$\overline{M_w}$ (g/mol)	PDI ($\overline{M_w}/\overline{M_n}$)	weight fraction	
			wt_{PS}	wt_{PI}
PS-*b*-PI(18/82)	68 300	1.02	0.181	0.819
PS-*b*-PI(37/63)	34 000	1.02	0.366	0.634
PS-*b*-PI(65/35)	23 500	1.05	0.648	0.352

3. Experimental Section

3.1. Sample Preparation. The PS-*b*-PI diblock copolymers used in our study were synthesized by anionic polymerization,[24] and their compositions and molecular weights were characterized. Two mixed bed columns (Polymer Lab., PL mixed C × 2) were used for the size exclusion chromatography (SEC) analysis, and the eluent was THF (HPLC grade). Chromatograms were recorded with a multiangle laser light scattering detector (Wyatt, mini-DAWN) and a refractive index detector (Wyatt, Opti-Lab). The compositions of the block copolymers were determined using a proton nuclear magnetic resonance (^{1}H NMR) spectrometer (Bruker, DPX-300). The measured weight-average molecular weights ($\overline{M_w}$) and PS block weight fractions (wt_{PS}) of the PS-*b*-PI copolymers are summarized in Table 1.

The silicon wafer substrates were cleaned by treating with piranha solution (concentrated H_2SO_4/30% H_2O_2 = 3/1 (v/v)) for 1 h and then washed with deionized water. Each diblock copolymer was dissolved in toluene at a concentration in the range 5−20 wt %, and this solution was then spin-coated onto a silicon wafer at 2000 rpm. The copolymer films were dried at room temperature in a vacuum for 12 h in order to remove the residual solvent completely. The copolymer films were then annealed in a vacuum oven at 120−160 °C for 1−3 days.

3.2. GISAXS Measurements. The GISAXS measurements were carried out at the 4C1 and 4C2 Beamlines[25] of the Pohang Accelerator Laboratory. A monochromatized X-ray radiation source of 8.05 keV (λ = 0.154 nm: λ, wavelength) and a two-dimensional charge-coupled device (2D CCD) detector (Roper Scientific, Trenton, NJ) were used. The sample-to-detector distance was 2500 mm. A set of aluminum foil strips was

employed as semitransparent beam stops because the intensity of the specular reflection from the substrate is much stronger than the intensity of GISAXS near the critical angle. Samples were mounted on a homemade *z*-axis goniometer equipped with a vacuum chamber. The incidence angle α_i of each X-ray beam was set in the range 0.20°−0.22°, which is between the critical angles of the copolymer films and the silicon substrate ($\alpha_{c,f}$ and $\alpha_{c,s}$). Scattering angles were corrected by the positions of X-ray beams reflected from the silicon substrate interface with changing incidence angle α_i and by a precalibrated polystyrene-*b*-polyethylene-*b*-polybutadiene-*b*-polystyrene (SEBS) block copolymer. Data were typically collected for 100−600 s.

4. Results and Discussion

4.1. HEX-Structured Microdomains. GISAXS measurements were carried out at $\alpha_i = 0.21°$ for films of the PS-*b*-PI(18/82) block copolymer with a PS block weight fraction of 0.18, which were prepared on silicon substrates with a topmost native oxide layer with various thicknesses in the range 85−1600 nm and then annealed at 140 °C for 3 days in a vacuum.

Figure 3a shows the 2D GISAXS pattern obtained for an 800 nm thick PS-*b*-PI(18/82) film; an AFM image of this film is shown in Figure 3b. The GISAXS pattern contains some diffraction spots with weakly developed semicircular lines. Taking into account the diffraction peaks due to the presence of the two X-ray beams, i.e., the transmitted and reflected beams discussed in section 2.1, we can analyze the GISAXS pattern. As can be seen on the right side of Figure 3a, the block copolymer film produces several diffraction spots, *R1*, *R2*, and *R3*, whose relative scattering vector lengths from the specular reflection position are 1, $\sqrt{3}$, and 2, respectively. These diffraction spots indicate that microdomains with a hexagonally packed cylinder (HEX) structure have formed in the PS-*b*-PI(18/82) film; their cylinder axes lie in the film plane (see model 1 in Figure 3c). Taking this HEX structure into account, the *R1*, *R2*, and *R3* spots can be assigned as the diffraction peaks of the {10}, {11}, and {21} planes, respectively, which were generated by the reflected X-ray beam, whereas the *T1* spot can be assigned as the diffraction peak of the {10} plane, which was generated by the transmitted X-ray beam. The $\alpha_{c,f}$ can be determined through an analysis of the out-of-plane scattering profile extracted at $2\theta_f = 0.35°$, indicating that the electron density of the film is 338 nm^{-3}; the electron density of the silicon substrate was found to be 699.5 nm^{-3} from $\alpha_{c,s}$ (see the $\alpha_f = \alpha_{c,f}$ and $\alpha_f = \alpha_{c,s}$ lines in Figure 3a).[9,13]

The GISAXS pattern also contains weak rings: each ring, a so-called Debye−Scherrer ring, links the diffraction spots from the same family of lattice planes with different orientations (see Figure 3a). The presence of these weak diffraction rings indicates that there is only a small population of HEX-structured microdomains randomly oriented along the cylinder axis in the PS-*b*-PI(18/82) film. The ring marked *A* is the diffraction generated by the outgoing reflected beam, whereas the ring marked *B* is the diffraction generated by the incoming beam (see the left side of Figure 3a). These results indicate that the majority of the HEX-structured domains are aligned with their {10} planes parallel to the film surface. This orientation is consistent with the results of Wang et al.[26] for Monte Carlo simulations of diblock copolymer thin films confined between two homogeneous surfaces.

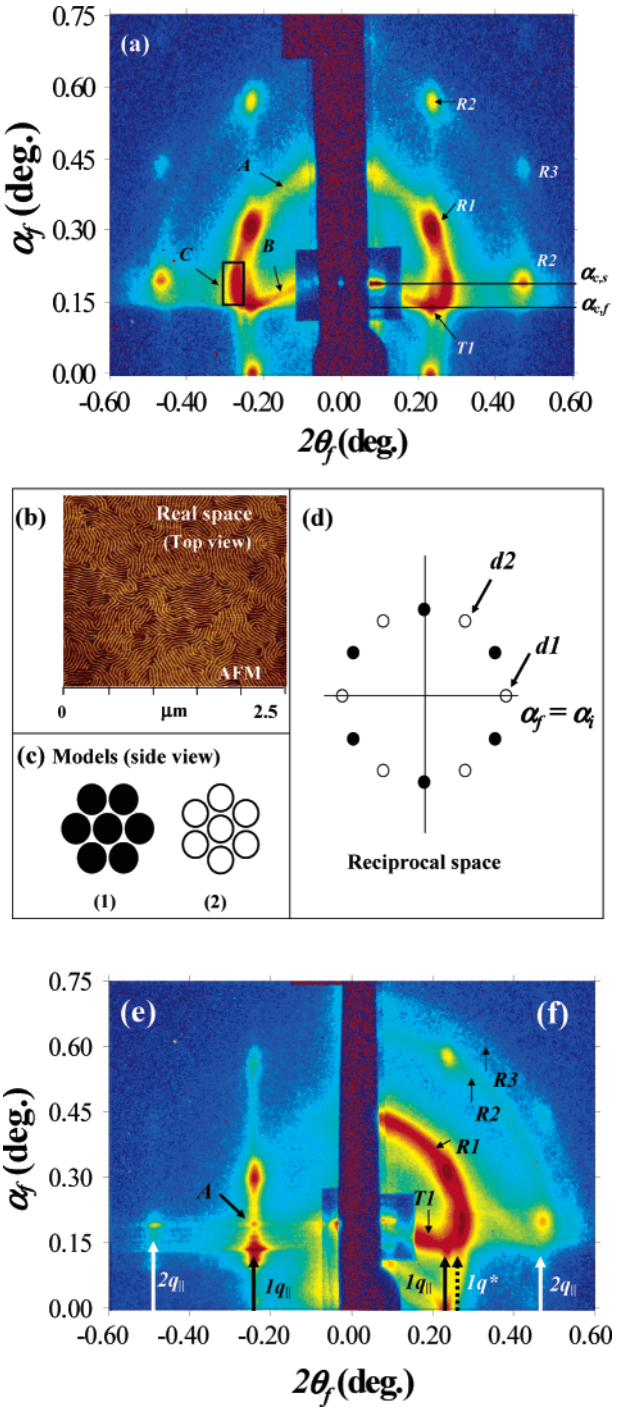

Figure 3. (a) GISAXS pattern measured at $\alpha_i = 0.21°$ for an 800 nm thick PS-*b*-PI(18/82) film deposited on a silicon substrate: *R* and *T* indicate the diffraction peaks due to the reflected and transmitted beams respectively; *1*, *2*, and *3* indicate the {10}, {11}, and {20} planes, respectively. (b) AFM image of the film in (a). (c) Two possible models of HEX-structured microdomains in the film of (a). (d) A schematic GISAXS pattern for HEX structures in the film plane, as generated by the reflected beam: filled spots are the diffraction peaks of a HEX structure without rotation [model 1 in (c)]; open spots are the diffraction peaks of a HEX structure with 30° rotation along the cylinder axis [model 2 in (c)]. (e) GISAXS pattern measured at $\alpha_i = 0.21°$ for a 400 nm thick PS-*b*-PI(18/82) film deposited on a silicon substrate. (f) GISAXS pattern measured at $\alpha_i = 0.21°$ for a 1600 nm thick PS-*b*-PI(18/82) film deposited on a silicon substrate.

In addition, there is a strong peak designated *C* on the left side of Figure 3a. One possibility is that this peak is due to HEX microdomains rotated by 30° along

the cylinder axis (see model 2 in Figure 3c), which are thus in relatively high population. If this is correct, peak *C* can be assigned as the (10) peak for the 30°-rotated HEX-structured microdomains, which is the diffraction designated *d1* on the right of Figure 3d. According to this assignment, another (10) peak, which is designated *d2* (Figure 3d), should also appear. However, this peak was not detected. Therefore, we conclude that peak *C* is a part of the diffraction ring, rather than a diffraction from 30°-rotated HEX-structured microdomains. The question then arises as to why *C* is so much brighter than the rest of the diffraction ring. To answer this question, consider the position (i.e., the α_f value) of *C*: it is located between $\alpha_{c,f}$ and $\alpha_{c,s}$. In GISAXS measurements, intense scattering generally takes place in the exit angle α_f region between $\alpha_{c,f}$ and $\alpha_{c,s}$ due to a type of standing wave phenomenon and total reflection at the interface between the film and the substrate. Taking this fact into account, the intense scattering at *C* is attributed to the significant increase in intensity of the diffraction ring that results from such grazing incidence effects.

Figure 3e shows the 2D GISAXS pattern of a 400 nm thick PS-*b*-PI(18/82) film obtained at 160 °C during a heating run at 2.0 °C/min. The scattering pattern contains no ring diffraction peaks. However, note that the GISAXS pattern of the 400 nm thick film contains ring diffraction peaks at room temperature but that their intensities were much weaker than those observed for the 800 nm thick film. Similar GISAXS patterns were observed for a 85 nm thick PS-*b*-PI(18/82) film (data not shown). These films produce much sharper diffraction spots (see the 1:2 relative peak positions designated by arrows with $1q_{||}$ and $2q_{||}$ along the in-plane direction in Figure 3e, which are different from those of the Debye−Scherrer rings appearing at intervals of 1, $\sqrt{3}$, and 2 for the 800 nm thick film). These results indicate that the HEX-structured microdomains in these thinner films are preferentially oriented with their {10} planes parallel to the film surface, and this occurs to a greater degree than in the 800 nm thick film. Moreover, this preferential orientation of the HEX-structured microdomains increases with heating to 160 °C.

In addition, Figure 3e shows there are modulated spots in the GISAXS pattern along the vertical line *A*, which appear between $\alpha_{c,f}$ and $\alpha_{c,s}$. These spots might not be measured when GISAXS peaks from domain spacings are sharp. However, such spots are often detected when scattering from a film's surface roughness is involved, which is strong along the in-plane direction and further enhanced between $\alpha_{c,f}$ and $\alpha_{c,s}$. Taking this fact into account, the observed high intensity of the spot designated by the thick arrow is attributed to surface scattering from the film, which has a certain degree of surface roughness.

Figure 3f displays the 2D GISAXS pattern of a 1600 nm thick film obtained at room temperature. The scattering measurements were extended for the film by carrying out a heating run up to 160 °C. However, the scattering pattern was found to be independent of temperature and time in the heating run, except for slight changes in the *d*-spacings (data not shown). As can be seen in Figure 3f, the scattering pattern contains ring diffraction peaks, with stronger intensities than those observed for the 800 nm thick film. An additional peak marked with a dotted arrow appears at the position $1q^*$, which is equivalent to the diffraction ring part *C* in Figure 3a; the relative length ratio of $1q^*$ to $2q_{||}$ is 1 to $\sqrt{3}$. These results indicate that as the film thickness increases, the orientations of the HEX-structured microdomains along the cylinder axis become disturbed, resulting in Debye−Scherrer rings in the scattering pattern.

However, the diffraction spots observed for the 400 nm thick film were astonishingly also detected in the scattering pattern of the 1600 nm thick film (Figure 3e,f), indicating that there is a high population of HEX-structured microdomains preferentially oriented along the {10} plane parallel to the film surface even in the 1600 nm thick film, with no preference for other orientations such as the 30°-rotated HEX structure (model 2 in Figure 3c). These results suggest that ordering and orientation effects of the substrate surface are likely to be present in PS-*b*-PI(18/82) films much thicker than 1600 nm.

Taken collectively, the results discussed so far suggest that increased populations of HEX-structured microdomains oriented with their {10} planes parallel to the film surface develop in thinner films. Moreover, this preferential orientation of the HEX-structured microdomains is enhanced in thinner films when they are heated to 160 °C.

To analyze the observed GISAXS patterns in more detail, we attempted to take the HEX structures into account in calculations of 2D GISAXS patterns using the GISAXS formula (eq 11) derived with the DWBA. In these GISAXS calculations, we required several parameters: the lattice parameter of the HEX structure is 37.9 nm, which was determined from the in-plane component $q_{||}$ of the (10) peak, with a standard deviation of 2.0 nm; $\alpha_i = 0.21°$ and 0.24° were chosen for the incoming X-ray beam. The calculated GISAXS patterns are shown in Figure 4.

Parts a and b of Figure 4 show the 2D GISAXS patterns calculated with $\alpha_i = 0.21°$ and 0.24°, respectively, for HEX-structured microdomains perfectly oriented with their {10} planes parallel to the film surface; the inset in Figure 4a shows the real-space model representing the HEX-structured microdomains that was used in the calculation of the GISAXS patterns. As can be seen from the comparison of the GISAXS patterns in Figure 4a,b with those in Figure 3, the calculated diffraction spots are found to be in good agreement with those in the measured scattering patterns. Note that the strips linking the neighboring peaks in Figure 4a,b result from the positional disordering of particles in the paracrystal model; variations in particle positions are allowed in the paracrystal model along the axis of the 2D hexagonal lattice, which result in the 6-fold strips. Such strips were also found in part in the GISAXS patterns obtained for the 400 and 800 nm thick copolymer films: the scattering pattern of the 400 nm thick film contains a 2-fold vertical strip (Figure 3e), whereas that of the 800 nm thick film has a relatively weak vertical strip (Figure 3a). No such strip was found in the scattering pattern of the 1600 nm thick film (Figure 3f). These comparisons indicate that the HEX-structured microdomains oriented along {10} planes parallel to the film surface have a limited coherent length along the direction normal to the film plane, which is dependent upon the film thickness. The limited coherent length of such in-plane oriented HEX structures along the out-of-plane direction of the film is possibly mainly caused by the air interface, which

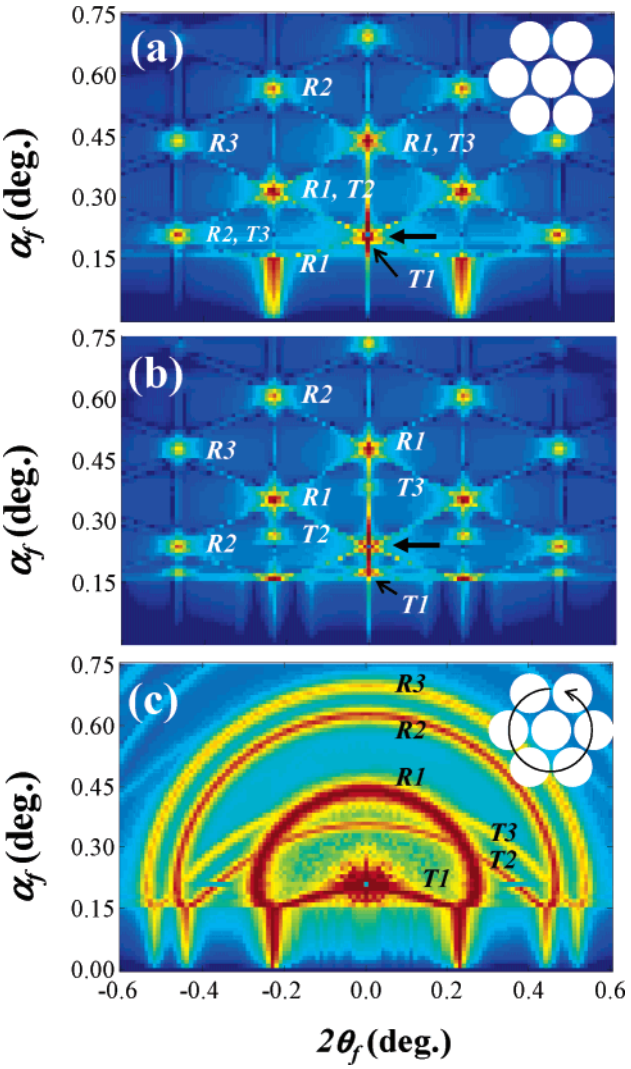

Figure 4. (a) GISAXS pattern calculated with $\alpha_i = 0.21°$ for HEX-structured microdomains perfectly oriented along the {10} plane parallel to the film plane (see the model in the inset) in a film deposited on a silicon substrate using the GISAXS formula (eq 20): the lattice unit cell parameter is 37.9 nm with a standard deviation of 2.0 nm, the wavelength λ of the X-ray beam is 0.154 nm, the electron densities of the film and the silicon substrate are 338 and 699.5 nm^{-3}, respectively, the length and radius of the cylinder are 180 and 18 nm, respectively, and the film thickness is 400 nm; the large arrow indicates the specular reflection of the reflected X-ray beam. *R* and *T* indicate the diffraction peaks due to the reflected and transmitted beams respectively; *1*, *2*, and *3* indicate the {10}, {11}, and {20} planes, respectively. The indices of the unlabeled spots in the half pattern are found by inverting those of the corresponding spots in the other half of the pattern. (b) GISAXS pattern calculated with $\alpha_i = 0.24°$ for the HEX structure in (a); all parameters in the calculation are same as those in (a); all labels are the same as those in (a). (c) GISAXS pattern calculated with $\alpha_i = 0.21°$ for HEX-structured microdomains randomly oriented along the cylinder axis in the film plane (see the model in the inset).

makes the HEX-structured microdomains unstable and disoriented.

In addition, as can be seen in Figure 4a,b, the GISAXS calculations clearly capture important characteristic features of the GISAXS measurements. First, the most intense diffraction peaks appear around the specular reflection position. Second, the high order diffraction peaks due to the reflected X-ray beam always appear as relatively intense peaks, whereas those due to the transmitted X-ray beam either appear weakly or do not appear at all. Third, the diffraction peaks due to the reflected beam are somewhat suppressed when $\alpha_i > \alpha_{c,s}$; larger α_i causes greater suppression of the diffraction. Fourth, the positions of the diffraction peaks due to the reflected and transmitted beams vary vertically, depending on the α_i value of the incoming X-ray beam. Furthermore, the diffraction peaks due to the reflected beam overlap or are separated from those due to the transmitted beam, depending on the α_i value of the incoming X-ray beam. For example, in the case where α_i is the same as the diffraction angle of the first-order diffraction peak, overlapping of the diffraction spots due to the transmitted and reflected X-ray beams occurs. Fifth, when the diffraction angles of the HEX-structured microdomains in the film are larger than the $\alpha_{c,s}$ value, the diffraction peaks due to the transmitted beam become more intense and can then be analyzed. However, as the diffraction angles decrease toward $\alpha_{c,f}$ and beyond, the diffraction peaks due to the transmitted X-ray beam are severely distorted and sometimes cannot be detected, which is due to the effects of refraction; in this case, the first-order diffraction could not be detected, but the second and higher diffraction peaks were observed (Figure 4b). The refraction effect is discussed in more detail in the next section. Finally, unlike those due to the transmitted beam, the diffraction peaks due to the reflected beam can be detected and then resolved regardless of their q_z component, which is one of the major advantages of the GISAXS technique.

Our summary of the GISAXS characteristics of this system suggests a guideline for measuring GISAXS patterns: changing the α_i value of the X-ray beam is absolutely necessary in order to resolve the resulting diffraction peaks; α_i can be varied between $\alpha_{c,f}$ and $\alpha_{c,s}$ in order to fully utilize the total reflection of the substrate. Note also that the GISAXS technique becomes difficult to apply if the electron density of the film is close to that of the substrate; thus, a substrate with an electron density higher than that of the film coated on top of the substrate is preferred in GISAXS measurements.

Figure 4c shows a 2D GISAXS pattern calculated with $\alpha_i = 0.21°$ for HEX-structured microdomains randomly oriented along the cylinder axis in the film plane (see the model in the inset). The calculated scattering pattern clearly shows diffraction rings with relative peak positions 1, $\sqrt{3}$, and 2, which are the structural characteristics of HEX-structured microdomains randomly oriented along the cylinder axis in the film plane (see the rings marked *R1*, *R2*, and *R3* in Figure 4c); these rings are due to the diffraction of the reflected X-ray beam. The calculated scattering pattern also shows the diffraction rings due to the transmitted X-ray beam (see the rings marked *T1* and *T2*). By comparing this calculated scattering pattern with the measured scattering pattern in Figure 3, it can be seen that the calculated diffraction rings are in good agreement with those observed in the measured scattering pattern.

Taking into consideration the GISAXS patterns calculated for the perfectly oriented and randomly oriented HEX structures (Figure 4), we conclude that the GISAXS patterns of the PS-*b*-PI(18/82) films (Figure 3) result from a mixture of structures, predominantly of preferentially well-oriented HEX-structured microdomains, but also of randomly oriented HEX-structured microdomains, where the orientations are with respect to the cylinder axis in the film plane. The proportions of these

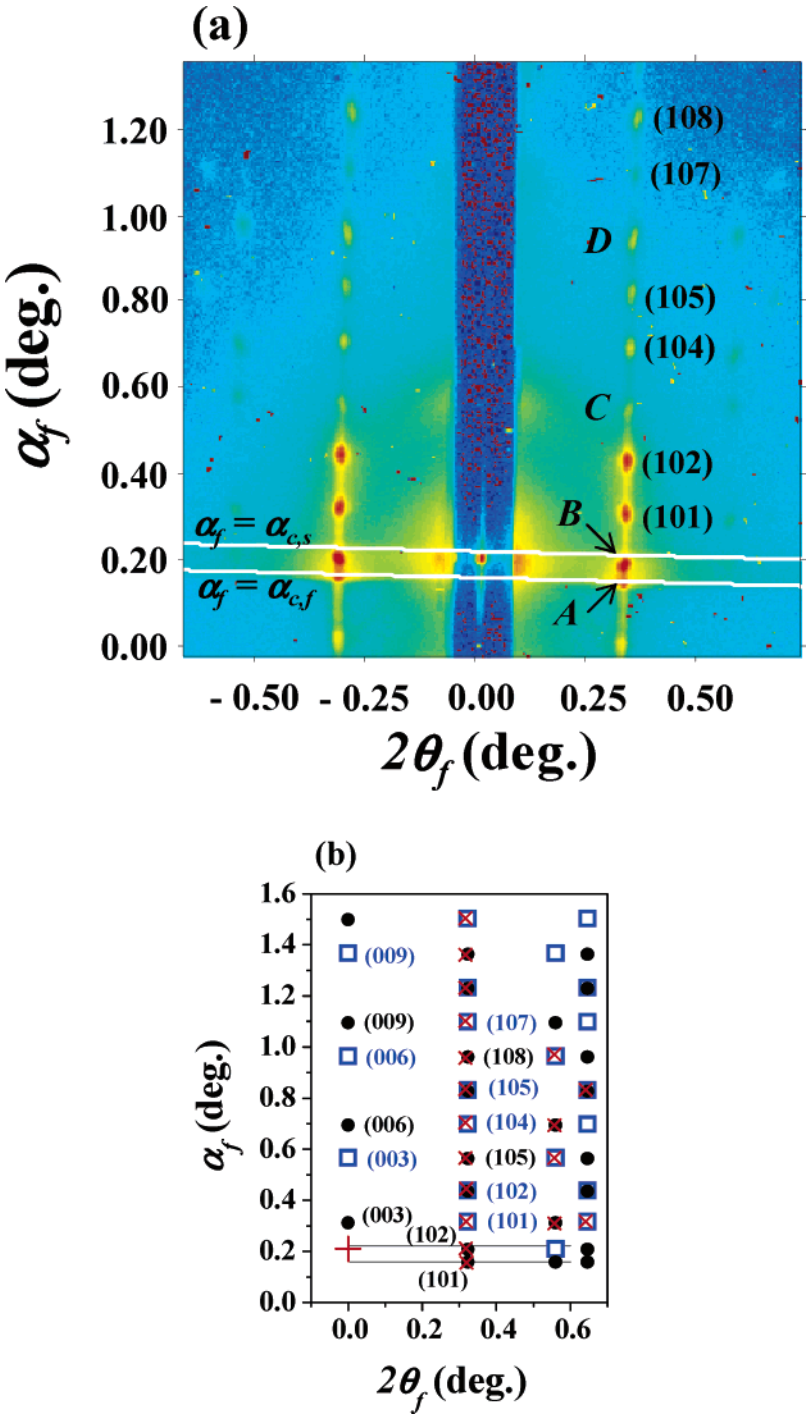

Figure 5. (a) GISAXS pattern measured at $\alpha_i = 0.21°$ for a 450 nm thick PS-*b*-PI(37/63) film deposited on a silicon substrate; the assignments of some diffraction peaks were made on the basis of an ABC stacked HPL structure. (b) A half of the GISAXS pattern calculated at $\alpha_i = 0.21°$ for hexagonal structured microdomains perfectly oriented along the {003} plane parallel to the film plane in a film deposited on a silicon substrate, using eqs 21−23; the lattice parameters are $a_H = 31.6$ nm and $c = 65.0$ nm, the wavelength λ of the X-ray beam is 0.154 nm, the electron densities of the film and the silicon substrate are 360 and 699.5 nm^{-3}, respectively, and the film thickness is 450 nm; open squares and filled circles denote diffraction peaks due to the reflected and transmitted X-ray beams, respectively; × symbols correspond to the measured peaks shown in (a); the cross indicates the specular reflection of the reflected X-ray beam. The two horizontal lines are $\alpha_f = \alpha_{c,s}$ (upper line) and $\alpha_f = \alpha_{c,f}$ (lower line).

two orientations of the HEX-structured microdomains are dependent on the film thickness, annealing temperature, and measurement temperature. Overall, the preferential orientation of the HEX-structured microdomains along the cylinder axis in the film plane is favored by thinner films, annealing at higher temperatures for a longer time, and a higher measurement temperature.

4.2. HPL-Structured Microdomains. A thin film of PS-*b*-PI(37/63) diblock copolymer with a PS block weight fraction of 0.366 was prepared on silicon substrates with a native oxide layer and then annealed at 120 °C for 1 day in a vacuum. Figure 5a shows a typical 2D GISAXS pattern obtained at $\alpha_i = 0.21°$ for the annealed block copolymer films with a thickness of 450 nm. The scattering pattern contains a number of sharp

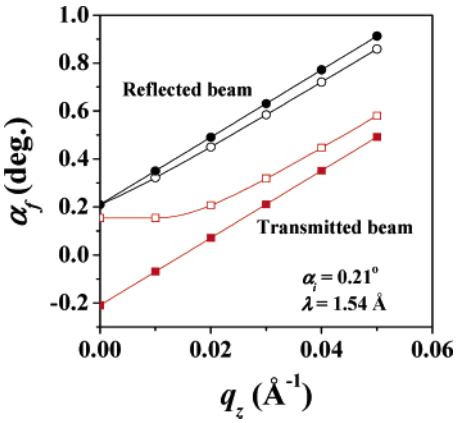

Figure 6. Relations between q_z and α_f of the diffraction peaks due to the reflected (circles) and transmitted (squares) X-ray beams: the filled and open symbols denote the diffraction peaks without and with correction for the refraction effect, respectively.

diffraction spots over a wide range of diffraction angles. In particular, there are a number of diffraction peaks located periodically along the q_z axis around $2\theta_f = 0.265°$; a lower number of diffraction spots also appear along the q_z axis around $2\theta_f = 0.517°$. These indicate that a well-ordered structure of microdomains is present in the film and that a certain lattice plane of the structure is aligned parallel to the film surface. The electron density of the film was determined to be 360 nm^{-3} from the out-of-plane scattering profile extracted at $2\theta_f = 0.25°$.

A PS-*b*-PI block copolymer with similar composition has been shown to be made up of a hexagonally perforated layer (HPL) structure of microdomains.[27,28] The perforations in such HPL structure has been reported to have an ABC stacked structure.[27] Assuming an ABC stacked structure for the ordered microdomains in the film, we attempted to assign the measured diffraction peaks. The scattering pattern and summarized peak assignments are shown in Figure 5a. Here we carried out the peak assignments by assuming that a majority of the diffraction peaks are generated by the reflected X-ray beam, since, as shown in the previous section, the diffraction peaks in the GISAXS pattern of HEX-structured microdomains in PS-*b*-PI(18/82) thin films are mostly produced by the reflected X-ray beam. Some diffraction peaks (for example, the peaks marked *A*−*D*) could not be assigned by considering only scattering due to the reflected beam; these peaks are due to the transmitted beam (see below). For the assumed ABC stacked structure, the lattice parameter a_H was determined to be 31.6 nm from the in-plane component $q_{||}$ (i.e., $2\theta_f$) value of the assigned (10*l*) peaks by using $a_H = 2\pi \cdot 2/\sqrt{3} q_{||,(10l)}$, whereas the other lattice parameter *c* was estimated to be 66.9 nm from the out-of-plane q_z components of those peaks. This value for *c* was further corrected by taking into account the refraction effect and was found to be 65.0 nm (see below).

To elucidate the origin of the peaks A−D, we need to consider the effect of refraction in the GISAXS measurements because this effect can be significant, particularly for the GISAXS pattern of the PS-*b*-PI(37/63) film with 360 nm^{-3} electron density, which has a microdomain structure on the scale of several tens of nanometers. Figure 6 shows the distortion of the diffraction peaks from the reflected and transmitted beams along the out-of plane direction (i.e., q_z direction) due to the refraction. There is a linear relationship between their scattering vector component q_z and exit angle α_f for both reflected and transmitted beams if the refraction effect is absent. When the refraction effect is taken into account, the diffractions from to the reflected beam produce deviations from the linear q_z and α_f relationship; the deviation becomes greater as q_z increases (the apparent *d*-spacing is smaller). The refraction effect causes a much greater deviation for the transmitted beam, and the deviation is much greater at small q_z (the apparent *d*-spacing is larger). In particular, in the case where a given *d*-spacing is large (at small q_z), the diffraction converges to $\alpha_{c,f}$, and the diffraction peaks from the transmitted beam cannot be resolved. Taking the refraction effect into account, the positions of the (10*l*) peaks assigned by assuming an ABC stacked structure were further corrected and then linearly fitted, providing a corrected hexagonal lattice parameter $c = 65.0$ nm.

On the basis of the determined hexagonal structure of $c = 65.0$ nm and $a_H = 31.6$ nm, we calculated the GISAXS patterns using the GISAXS formula (eqs 21−23). In this calculation, the α_i of the incoming X-ray beam was 0.21°. In addition, the *c*-axis was treated as oriented along a direction normal to the film surface, whereas the other two axes were randomly aligned in the film plane, as determined from the observed multiple (10*l*) peaks described above.

The calculated GISAXS pattern of the HPL structure is shown in Figure 5b. By comparison of this pattern with the experimental pattern, all the diffraction peaks generated by the reflected X-ray beam were confirmed (see Figure 5a,b). Furthermore, the diffraction peaks marked *A*−*D* are assigned as (101), (102), (105), and (108) peaks generated by the transmitted X-ray beam. However, some diffraction peaks in the large α_f and $2\theta_f$ region of the calculated scattering pattern were not observed in the measured scattering pattern, presumably because of their weak intensities. The diffraction peaks of the calculated scattering pattern are thus overall well matched with those of the measured scattering pattern.

Our results lead collectively to the conclusion that in 120 °C annealed PS-*b*-PI(37/63) films of 450 nm thickness deposited on silicon substrates with a native oxide layer, there is a high population of HPL-structured microdomains in a preferential orientation of their *c*-axis along a direction normal to the film plane.

Note that the diffraction peaks of the measured GISAXS pattern for the HPL structure also feature vertical strips (i.e., vertical elongations), as was observed in the scattering pattern for the HEX structure described in the previous subsection (Figure 3e). This indicates that the positional disorder of the preferentially oriented HPL structure is greater along the out-of-plane direction of the film than in the film plane, which is attributed to the thin film thickness.

As described above, we have demonstrated that the use of the GISAXS technique with the derived GISAXS formula as a data analysis engine is a very powerful tool for determining the HPL structure of diblock copolymer thin films coated onto substrates. In fact, HPL-structured microdomains in thin films coated onto substrates cannot be characterized using conventional techniques with a scanning mode along the film plane, such as transmission SAXS, AFM, and TEM, because these structures tend to align in a layer parallel to the

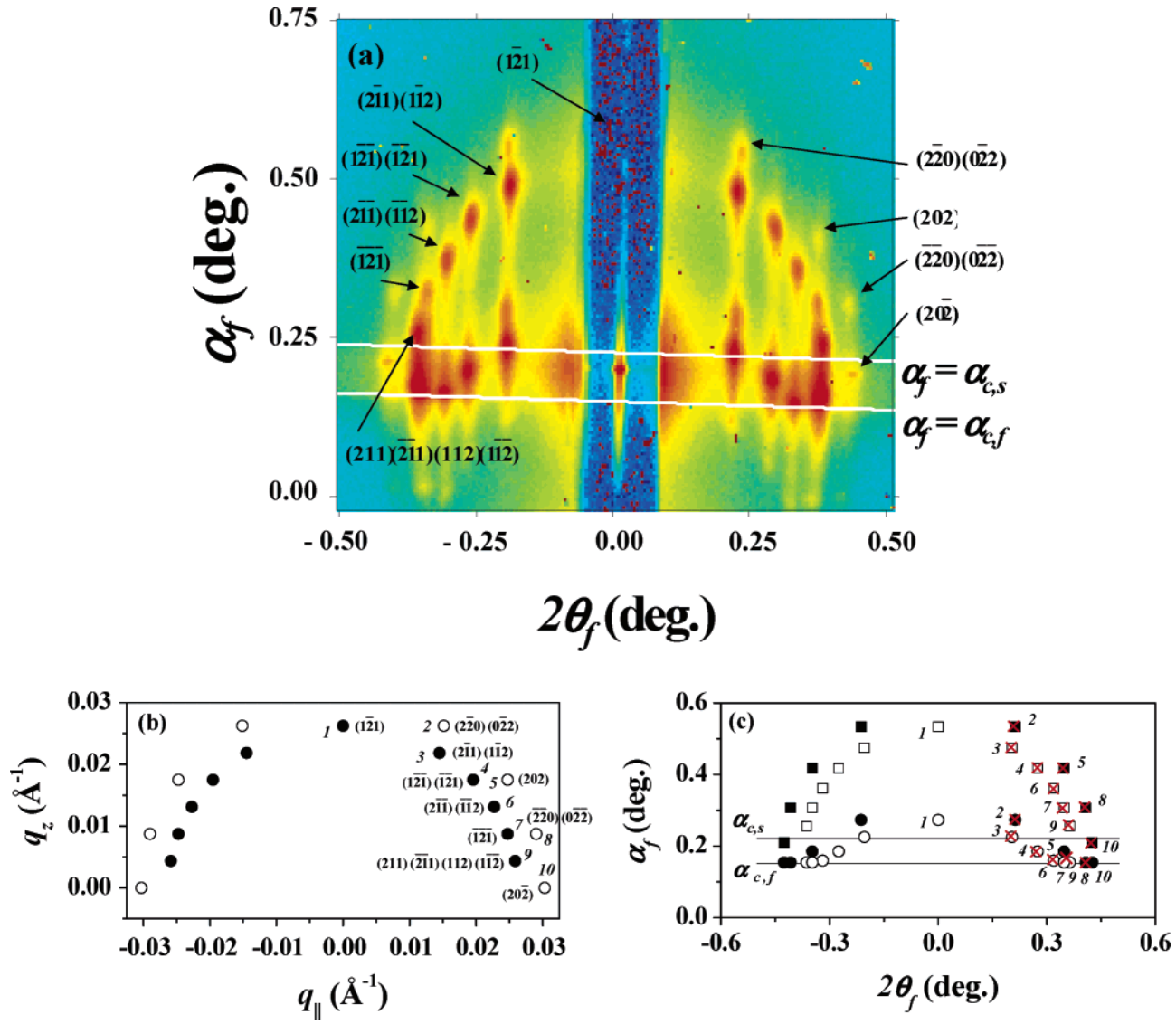

Figure 7. (a) GISAXS pattern obtained at $\alpha_i = 0.21°$ for a 650 nm thick PS-*b*-PI(65/35) film deposited on a silicon substrate; the assignments of some diffraction peaks were made on the basis of a gyroid structure whose {121} plane is oriented parallel to the film plane. (b) The upper half of the TSAXS pattern calculated for a gyroid structure with a lattice parameter of 58.7 nm: the wavelength λ of the X-ray beam is 0.154 nm. Open symbols denote the diffraction peaks of the {121} plane and filled symbols indicate those of the {220} plane. The indices of the unlabeled spots in the left quadrant are found by inverting those of the corresponding spots in the right quadrant. (c) GISAXS pattern calculated with $\alpha_i = 0.21°$ for gyroid-structured microdomains perfectly oriented along the {121} plane parallel to the in-plane of a film deposited on a silicon substrate; the lattice parameter is 58.7 nm, the wavelength λ of the X-ray beam is 0.154 nm, the electron densities of the film and the silicon substrate are 340 and 699.5 nm^{-3}, respectively, and the film thickness is 650 nm; squares and circles denote the diffraction peaks due to the reflected and transmitted X-ray beams, respectively; open symbols denote the diffraction peaks of the {121} plane and filled symbols indicate those of the {220} plane; × symbols correspond to the measured diffraction peaks shown in (a). The indices of the unlabeled spots in the left half are found by inverting those of the corresponding spots in the right half.

film surface and indeed look like a hexagonally packed 2D cylinder structure.

4.3. Gyroid-Structured Microdomains. GISAXS measurements were carried out at $\alpha_i = 0.21°$ for 650 nm thick films of PS-*b*-PI(65/35) diblock copolymer with a PS block weight fraction of 0.648, which were prepared on silicon substrates with native oxide layers and then annealed at 160 °C for 1 day in a vacuum. Figure 7a shows one of the GISAXS patterns, which contains a number of diffraction spots over a wide range of diffraction angles and also very weak diffraction rings in the low diffraction angle region; in particular, diffraction peaks appear along the q_z axis at around $2\theta_f = 0.22°$, 0.29°, 0.33°, 0.37°, and 0.44°.

The GISAXS pattern well matches with (121) diffraction spots as well as (220) diffraction spots, confirming that in the diblock copolymer film gyroid-structured microdomains develop with a preferential orientation along the direction normal to the film plane. For the gyroid structure, the lattice parameter a_G was determined to be 58.7 nm from the in-plane component $q_{\|}$ (i.e., $2\theta_f$) value of the assigned (20$\bar{2}$) peaks, which is not distorted by the refraction effect, by using $a_G = 2\pi \cdot 2\sqrt{2}/q_{\|,(20\bar{2})}$. The *d*-spacing of the first-order peak of the {121} plane was estimated to be 23.9 nm. In addition, the electron density of the film was determined to be 340 nm^{-3} from the out-of-plane scattering profile extracted at $2\theta_f = 0.18°$.

Taking the preferential orientation of the gyroid structure and its lattice parameter into account, we attempted to generate its TSAXS pattern in order to

deepen our understanding of the measured GISAXS pattern. The calculated TSAXS pattern is shown in Figure 7b. Only the first order peaks from the {121} and {220} planes were calculated because the intensities of the other higher order peaks are very weak. In the upper half of the calculated pattern, half the 24 permutation peaks for the {211} planes are shown; the other half of those permutation peaks appear in the lower half of the pattern, which are identical to those corresponding spots in the upper half as a result of rotational symmetry (the lower half is not shown). Half the 12 permutation peaks for the {220} planes are additionally shown in the pattern; the other half of those permutation peaks appears in the lower half of the pattern (the lower half is not shown). In these calculations, it was also found that the TSAXS pattern is identical when the gyroid-structured microdomains are randomly oriented around either the [121] or [112] lattice vectors, both of which are normal to the {121} plane. Overall, the calculated diffraction spots are comparable with those generated by the reflected beam in the measured GISAXS pattern (Figure 7a,b), except for some differences in the *d*-spacings. These results confirm that in the PS-*b*-PI(65/35) film, well-developed gyroid-structured microdomains formed with their {121} planes preferentially oriented parallel to the film plane. This type of TSAXS pattern was reported for poly(oxyethylene)-templated silica thin films dip-coated onto aluminized Kapton substrates.[29] The gyroid structure of this silica system resulted in (211) diffraction spots along the inner ellipse and also (220) diffraction spots along the outer ellipse of the SAXS pattern, indicating that the gyroid structure randomly orients around the $[1\bar{2}1]$ lattice vector, which is normal to the X-ray beam in the SAXS measurement.

For the gyroid structure with $a_G = 58.7$ nm preferentially oriented along a direction normal to the film surface, we attempted to calculate its GISAXS pattern in the same manner used for the HPL structure, as described in the previous subsection. The calculated GISAXS pattern is shown in Figure 7c. By comparison of this pattern with the experimental pattern, all the diffraction peaks generated by the reflected X-ray beam were confirmed (see Figure 7a,c). Furthermore, some other diffraction peaks of Figure 6a, which did not appear in the calculated TSAXS pattern, are found in the calculated GISAXS pattern (Figure 7c), which were generated by the transmitted X-ray beam. In particular, the calculated GISAXS pattern clearly shows the $(1\bar{2}1)$ peaks whose vector is normal to the film surface, as seen previously in the calculated TSAXS pattern; the $(1\bar{2}1)$ peaks were not discernible in the measured scattering pattern because they were shaded by the beam stop. Overall, the diffraction peaks of the calculated scattering pattern are well matched with those of the measured scattering pattern. These results lead to the conclusion that in 160 °C annealed PS-*b*-PI(65/35) films of 650 nm thickness deposited on silicon substrates with a native oxide layer, well-developed gyroid-structured microdomains formed with their {121} planes preferentially oriented parallel to the film plane.

Note also that the diffraction peaks of the measured GISAXS pattern of the gyroid structure also feature vertical strips (i.e., vertical elongations) as observed in the scattering patterns of the HEX and HPL structures (Figures 3c and 5a). This indicates that the positional disorder of the preferentially oriented gyroid structure in the film is greater along the out-of-plane direction than in the film plane, which is attributed to the thin film thickness.

5. Conclusions

The GISAXS patterns of structures in a thin film on a substrate are complicated by the reflection and refraction effects, which do not occur in conventional TSAXS. A GISAXS formula was derived to describe such complicated scattering under the DWBA formalism. The simplified GISAXS formula, eq 11, is useful when the phase of the scattered beam amplitude (eq 7) is not a critical issue, for example in the analysis of lattice structure by examining peak positions. This formula enables the calculation of GISAXS patterns by simply integrating all existing intensity forms of SAXS formulas or numerical forms into the formula. On the other hand, when phase information is required and the amplitude form of the scattering formula is known, the amplitude form of the GISAXS formula (eq 7; eq 9) can be used.

Using the derived GISAXS formula, the GISAXS patterns obtained for PS-*b*-PI diblock copolymer thin films with various morphologies (HEX, HPL, and gyroid) deposited on silicon substrates with a native oxide layer were characterized quantitatively. The full analyses demonstrated that the GISAXS technique is a very powerful tool for determining the morphologies of polymer thin films coated onto substrates, which is not possible using conventional techniques such as TSAXS, AFM, and TEM, which employ scanning modes along the film plane.

The GISAXS analyses found that the HEX, HPL, and gyroid structures developed in the PS-*b*-PI diblock copolymer films deposited on silicon substrates each have a unique characteristic orientation, depending on their composition: (i) the {10} plane of the HEX structure in the PS-*b*-PI(18/82) film is oriented parallel to the film plane; (ii) the {003} plane of the HPL structure in the PS-*b*-PI(37/63) film is oriented parallel to the film plane; (iii) the {121} plane of the gyroid structure in the PS-*b*-PI(65/35) film is oriented parallel to the film plane. These preferential orientations arise for the diblock copolymer films spin-coated onto silicon substrates, which have previously been reported only for shear-oriented bulk samples of diblock copolymers. These structures' preferential orientations are attributed to the positive cooperation of the interfacial interaction between the diblock copolymers and the silicon substrate with a native oxide layer as well as to the confinement of the thin film. Moreover, all the structured microdomains in the diblock copolymer thin films were found to have larger displacements in their crystallographic positions along the out-of-plane direction than along the film plane, which is attributed to the thinness of the films and the air interface. In addition, considering the crystallographic planes of the layers in the three morphologies (HEX, HPL, and gyroid) of our study, their transition mechanisms seem to be consistent with those in the bulk reported in the literature.

Acknowledgment. This study was supported by the Center for Integrated Molecular Systems (Korea Science and Engineering Foundation) and by the Ministry of Education (BK21 Program). Synchrotron GISAXS measurements were supported by the Ministry of Science & Technology and the POSCO.

References and Notes

(1) (a) Bates, F. S.; Schulz, M. F.; Khandpur, A. K.; Foerster, S.; Rosedale, J. H. *Faraday Discuss.* **1995**, *98*, 7. (b) Hashimoto, T. *Macromol. Symp.* **2001**, *174*, 69. (c) Leibler, L. *Macromolecules* **1980**, *13*, 1602. (d) Lodge, T. P.; Pudil, B.; Hanley, K. J. *Macromolecules* **2002**, *35*, 4707. (e) Matsen, M. W.; Schick, M. *Macromolecules* **1994**, *27*, 4014.

(2) Mansky, P.; Chaikin, P.; Thomas, E. L. *J. Mater. Sci.* **1995**, *30*, 1987.

(3) (a) Park, M.; Harrison, C.; Chaikin, P. M.; Register, R. A.; Adamson, D. H. *Science* **1997**, *276*, 1401. (b) Chou, S. Y.; Krauss, P. R.; Renstrom, P. J. *J. Vac. Sci. Technol. B* **1996**, *14*, 4129. (c) Herrninghaus, S.; Jacobs, K.; Mecke, K.; Bischof, J.; Fery, A.; Ibn-Elfraj, M.; Schlagowski, S. *Science* **1998**, *282*, 916. (d) Spatz, J. P.; Roescher, A.; Sheiko, S.; Krausch, G.; Moeller, M. *Adv. Mater.* **1995,** *7*, 731. (e) Ge, S.; Takahara, A.; Kajiyama, T. *Langmuir* **1995**, *11*, 1341.

(4) (a) Henkee, C. S.; Thomas, E. L.; Fetters, L. J. *J. Mater. Sci.* **1988**, *23*, 1685. (b) Anastasiadis, S. H.; Russell, T. P.; Satija, S. K.; Majkrzak, C. F. *Phys. Rev. Lett.* **1989**, *62*, 1852. (c) Radzilowski, L. H.; Carvalho, B. L.; Thomas, E. L. *J. Polym. Sci., Part B: Polym. Phys.* **1996**, *34*, 3081.

(5) (a) Schaffer, E.; Thurn-Albrecht, T.; Russell, T. P.; Steiner, U. *Nature (London)* **2000**, *403*, 874. (b) Rockford, L.; Liu, Y.; Mansky, P.; Russell, T. P.; Yoon, M.; Mochrie, S. G. J. *Phys. Rev. Lett.* **1999**, *82*, 2602.

(6) Segalman, R. A.; Hexemer, A.; Kramer, E. J. *Macromolecules* **2003**, *36*, 6831.

(7) (a) Holy, V.; Pietsch, U.; Baumbach, T. *High-Resolution X-ray Scattering from Thin Films and Multilayers*; Springer-Verlag: Berlin, 1999. (b) Sinha, S. K.; Sirota, E. B.; Garoff, S.; Stanley, H. B. *Phys. Rev. B* **1988**, *38*, 2297.

(8) Rauscher, M.; Salditt, T.; Spohn, H. *Phys. Rev. B* **1995**, *52*, 16855.

(9) (a) Lee, B.; Park, Y.-H.; Hwang, Y.-T.; Oh, W.; Yoon, J.; Ree, M. *Nat. Mater.* **2005**, *4*, 147. (b) Lee, B. Ph.D. Thesis, Pohang Univeristy of Science & Technology, Phang, Korea, 2003. (c) Lee, B.; Oh, W.; Hwang, Y.; Park, Y.-H.; Yoon, J.; Jin, K. S.; Heo, K.; Kim, J.; Kim, K.-W.; Ree, M. *Adv. Mater.* **2005**, *17*, 696.

(10) Omote, K.; Ito, Y.; Kawamura, S. *Appl. Phys. Lett.* **2003**, *82*, 544.

(11) Lazzari, R. *J. Appl. Crystallogr.* **2002**, *35*, 406.

(12) (a) Gracin, D.; Dubcek, P.; Zorc, H.; Juraic, K. *Thin Solid Films* **2004**, *459*, 216. (b) Winans, R. E.; Vajda, S.; Lee, B.; Riley, S. J.; Seifert, S.; Tikhonov, G. Y.; Tomczyk, N, A. *J. Phys. Chem. B* **2004**, *108*, 18105.

(13) Lee, B.; Yoon, J.; Oh, W.; Hwang, Y.; Heo, K.; Jin, K. S.; Kim, J.; Kim, K.-W.; Ree, M. *Macromolecules*, in press.

(14) Gibaud, A.; Grosso, D.; Smarsly, B.; Baptiste, A.; Bardeau, J. F.; Babonneau, F.; Doshi, D. A.; Chen, Z.; Jeffrey Brinker, C.; Sanchez, C. *J. Phys. Chem. B* **2003**, *107*, 6114.

(15) (a) Vignaud, G.; Gibaud, A. Wang, J.; Sinha, S. K.; Daillant, J.; Grubel, G.; Gallot, Y. *J. Phys.: Condens. Matter* **1997**, *9*, L125.

(16) Mueller-Buschbaum, P. *Anal. Bioanal. Chem.* **2003**, *376*, 3.

(17) (a) Smilgies, D.-M.; Busch, P.; Posselt, D.; Papadakis, C. M. *Synchrotron Rad. News* **2002**, *15*, 35. (b) Busch, P.; Smilgies, D.-M.; Posselt, D.; Kremer, F.; Papadakis, C. M. *Macromol. Chem. Phys.* **2003**, *204*, F18. (c) Du, D.; Li, M.; Douki, K.; Li, X.; Garcia, C. B. W.; Jain, A.; Smilgies, D.-M.; Fetters, L. J.; Gruner, S. M.; Wiesner, U.; Ober, C. K. *Adv. Mater.* **2004**, *16*, 953. (d) Li, M.; Douki, K.; Goto, K.; Li, X.; Coenjarts, C.; Smilgies, D.-M.; Ober, C. K. *Chem. Mater.* **2004**, *16*, 3800. (e) Xu, T.; Goldbach, J. T.; Misner, M. J.; Kim, S.; Gibaud, A.; Gang, O.; Ocko, B.; Guarini, K. W.; Black, C. T.; Hawker, C. J.; Russell, T. P. *Macromolecules* **2004**, *37*, 2972.

(18) (a) Renaud, G.; Lazzari, R.; Revenant, C.; Barbier, A.; Noblet, M.; Ulrich, O.; Leroy, F.; Jupille, J.; Borencztein, Y.; Henry, C. R.; Deville, J.-P.; Scheurer, F.; Mane-Mane, J.; Fruchart, O. *Science* **2003**, *300*, 1416. (b) Revenant, C.; Leroy, F.; Lazzari, R.; Renaud, G.; Henry, C. R. *Phys. Rev. B* **2004**, *69*, 035411.

(19) (a) Parratt, L. G. *Phys. Rev.* **1954**, *95*, 359. (b) Schlomka, J.-P.; Tolan, M.; Schwalowsky, L.; Seeck, O. H.; Stettner, J.; Press, W. *Phys. Rev. B* **1995**, *51*, 2311.

(20) Pedersen, J. S. *J. Appl. Crystallogr.* **1994**, *27*, 595.

(21) Pedersen, J. S. *Adv. Colloid Interface Sci.* **1997**, *70*, 171.

(22) Busson, B.; Doucet, J. *Acta Crystallogr.* **2000**, *A56*, 68.

(23) (a) Hashimoto, T.; Kawamura, T.; Harada, M.; Tanaka, H. *Macromolecules* **1994**, *27*, 3063. (b) Matsuoka, H.; Tanaka, H.; Hashimoto, T.; Ise, N. *Phys. Rev. B* **1987**, *36*, 1754.

(24) (a) Kwon, K.; Lee, W.; Cho, D.; Chang, T. *Korea Polym. J.* **1999**, *7*, 321. (b) Lee, W.; Cho, D. Y.; Chang, T. Y.; Hanley, K. J.; Lodge, T. P. *Macromolecules* **2001**, *34*, 2353.

(25) Bolze, J.; Kim, J.; Huang, J.-Y.; Rah, S.; Youn, H. S.; Lee, B.; Shin, T. J.; Ree, M. *Macromol. Res.* **2002**, *10*, 2.

(26) Wang, Q.; Nealey, P. F.; de Pablo, J. J. *Macromolecules* **2001**, *34*, 3458.

(27) (a) Ahn, J.-H.; Zin, W.-C. *Macromolecules* **2000**, *33*, 641. (b) Zhu, L.; Huang, P.; Chen, W. Y.; Weng, X.; Cheng, S. Z. D.; Ge, Q.; Quirk, R. P.; Senador, T.; Shaw, M. T.; Thomas, E. L.; Lotz, B.; Hsiao, B. S.; Yeh, F.; Liu, L. *Macromolecules* **2003**, *36*, 3180.

(28) Vigild, M. E.; Almdal, K.; Mortensen, K.; Hamley, I. W.; Fairclough, J. P. A.; Ryan, A. J. *Macromolecules* **1998**, *31*, 5702.

(29) Hayward, R. C.; Alberius, P. C. A.; Kramer, E. J.; Chmelka, B. F. *Langmuir* **2004**, *20*, 5998.

MA047562D